3D dose reconstruction using an in-house radioluminescence imaging system

M. Jia [1], Y. Yang [1], L. Wang [1] and L. Xing[1]

1 Department of Radiation Oncology, Stanford University, Stanford, CA94305, USA

JULY 12–16 2020 VIRTUAL
JOINT AAPM | COMP MEETING
EASTERN TIME [GMT-4]

INTRODUCTION

Rapid development in precision radiation therapy dramatically increases the demands for accurate and efficient pre-treatment dosimetric verification. Currently, electronic portal imaging device (EPID) is commonly used for the application due to its high-resolution characteristics and ease of use. However, EPID dosimetry solution does not provide in-phantom dosimetric information and are not available in certain clinical treatment systems. Here, we propose a dose verification method using a camera-based radioluminescence imaging system (CRIS) combined with a deep learning-based signal processing technique. The CRIS consists of a cylindrical chamber coated with scintillator material on the inner surface of the cylinder, coupled with a hemispherical mirror and a digital camera at two ends. After training, the deep learning model was used for image-to-dose conversion to provide dose prediction at multiple depths from a single CRIS image.

AIM

1, Develop the first volumetric camera-based radioluminescence imaging system for co-planar radiation beam detection

2, Investigate a deep-learning-based image-dose conversion approach to offer water-based dose at different depths.

3, Demonstrate the performance of developed system for clinical application on IMRT treatment plans.

METHOD

1. Design of radioluminescence imaging system

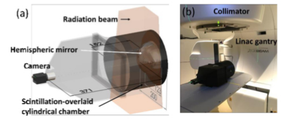

Fig. 1 (a) Schematic diagram of the developed CRIS phantom, and (b) experimental setup. The system consists of a cylindrical receptor with its inner surface coated with scintillator, a hemispheric mirror mounted at the cylinder end and a camera at the opposite end to capture the luminescence signals from the inner surface of the cylinder. The main dimensions are indicated in unit of millimeter.

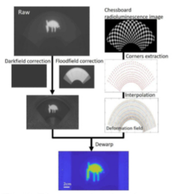

Fig. 2. Diagram showing the calibration procedure of CRIS image.

Hardware design of the radioluminescence imaging system is shown in Figure 1. The inner surface of a 3D printed cylindrical chamber is coated with a Gd_2O_2S-based scintillator material, which emits 545nm light upon interaction with the megavoltage (MV) photons [1,2]. The system was sequentially calibrated to compensate for any geometric restoration, dark-field and flood-field corrections. To perform image restoration, a chessboard was overlaid to the scintillator sheet and the captured scintillation image was used to extract deformable field for the subsequent affine transform. A diagram showing the calibration process is presented in Fig. 4. Calibrated images still suffer from the blurring and mirror-glare issues caused by light scattering, which will be mitigated using the deep learning model.

2. Deep learning model for image-dose conversion

Figure 3 shows the pipeline of the proposed fGAN, which takes advantages of the powerful adversarial learning mechanism in the prediction of dose maps. While dose maps at different depths are deemed to belong to different image domains, our goal is to train a single network that learns a one-to-many domain translation. In brief, the architecture consists of two identical generators (G_1 and G_2) and two discriminators (D_1 and D_2). G_1 takes input from both radioluminescence image and target domain labels (c_n) to synthesize dose maps at multiple depths. By passing a predicted dose map and the corresponding source label (c_0) into G_2, a radioluminescence image is reconstructed and used to formulate a cycle consistency loss. In fact, an identical G is used for both G_1 and G_2. Meanwhile, the discriminators play dual roles: a real/fake identifier and a domain classifier. An identical discriminator (D) is employed for both D_1 and D_2.

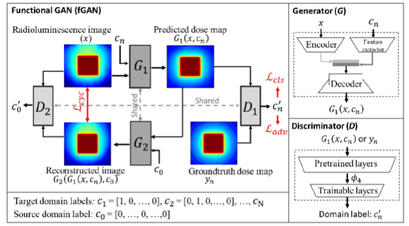

Fig. 3 The architecture of the proposed fGAN, consisting of two identical generators (G_1 and G_2) and two identical discriminators (D_1 and D_2). G_1 takes input from both radioluminescence image x and a target domain label vector ($c_n|n>0$) to a synthesize dose map at a desirable depth, i.e., $G_1(x, c_n)$. By passing a predicted target image and a source domain label c_0 into G_2, the source image is reconstructed, i.e., $G_2(G_1(x, c_n), c_0)$ and used to formulate a cycle consistency loss $\mathcal{L}_{cyc}$. The discriminators play dual roles: (1) a real/fake identifier, which contributes to $\mathcal{L}_{adv}$, and (2) a domain classifier to evaluate the similarity between the predicted dose map and the ground truth at every depth, which contributes to $\mathcal{L}_{clc}$.

- **Loss functions**

In fGAN, there are three loss functions involved: a perceptual adversarial loss $\mathcal{L}_{adv}$, a classification loss $\mathcal{L}_{cls}$, and a cycle consistency loss $\mathcal{L}_{cyc}$. the total objective is

$$\begin{cases} L_D = -L_{adv} + \lambda_{cls} L_{cls} \\ L_G = L_{adv} + \lambda_{cls} L_{cls} + \lambda_{cyc} L_{cyc} \end{cases}$$

where λ_{cls} and λ_{cyc} are hyper parameters that balance the contributions from classification loss and consistency loss, respectively.

- **Training data collection**

A LINAC (Varian Clinac 2100 CD, Varian Medical Systems, USA) equipped with Millennium MLC was used for all the experiments with photon energy of 6 MV and dose rate of 600 monitor units per minute (MU/min). Dose calculations were conducted in the Eclipse™ (Varian Medical Systems, Palo Alto, California) using the anisotropic analytical algorithm (version 15.6.05). The calculation was performed on a cubic water phantom (45 × 45 × 45 cm³) constructed in the TPS with a source-to-surface distance (SSD) of 100 cm.

The training dataset is composed of 58 shapes (see Fig. 4). The measurement was taken for multiple collimator rotations ranging from 0° to 180° at a step size of 15°. That is, at 12 MLC rotations angles, 12 × 58 images were taken in all. The gantry angle was fixed to 0° during the data collection process. Dose was calculated in TPS at the depth of 1.5cm, 5cm and 10cm, and the model was trained for the three depths.

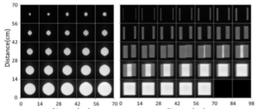

Fig. 4 Training dataset includes MLC-defined (a) circular and (b) comb-like fields. The two designs are intended for learning disentangled features regarding content and edge. These images presented were collected by using the CRIS.

RESULTS

Dose maps were predicted and verified for 1.5 cm, 5 cm and 10 cm depths in water. The test dataset consists of regular fields and a clinical IMRT case. The regular fields include a set of square fields: 2×2 cm², 4×4 cm², 6×6 cm², 8×8 cm² and 10×10 cm². The clinical prostate case contains seven fields with a total of seventy-seven segments. The predicted dose maps were evaluated by comparing to the corresponding TPS calculations in terms of gamma index (Υ). The gamma passing rates were calculated (Υ_{pass}) using gamma criteria of 1% (global intensity) /1 mm (distance-to-agreement) and 2%/2 mm with a low-dose cut-off threshold value of 10%.

1. Dose prediction for regular fields

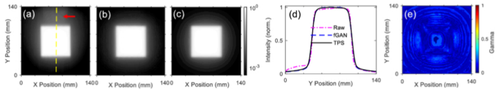

Fig. 5. Dose prediction for a 6×6cm² open field at a water depth of 10 cm. (a) The input portal image collected from our CRIS, (b) predicted dose map, (c) TPS calculation, (d) intensity profiles along the yellow dashed line in (a), and (e) gamma map of the prediction (2% / 2mm). Images are displayed in logscale.

Table I Gamma analysis of predictions and original radioluminescence images (in bracket) for regular open fields

	Depth	2×2 cm²	4×4 cm²	6×6 cm²	8×8 cm²	10×10cm²
1%/ 1mm	1.5 cm	99.5%(92.1%)	99.9%(81.0%)	100%(57.4%)	100%(48.2%)	100%(30.6%)
	10cm	99.7%(75.1%)	99.9%(69.9%)	100%(69.8%)	99.3%(60.1%)	99.9%(28.4%)
2%/ 2mm	1.5 cm	100%(98.7%)	100%(96.3%)	100%(78.8%)	100%(86.7%)	100%(41.8%)
	10 cm	100%(98.2%)	100%(97.5%)	100%(98.0%)	100%(91.2%)	100%(52.8%)

Figure 5 shows an example of 6×6cm² field. The images are displayed in log-scale to reveal the details in the penumbra regions. In this case, the mirror-glare artifacts can be observed on top of radioluminescence images, as indicated with a red arrow in Fig. 5(a). In the cross-beam profiles shown in Fig. 5(d), the artifacts lead to a 10% deviation relative to the maximum dose. These artifacts are eliminated in the predicted dose map (Fig. 5(b)), which has a 100% Υ_{pass} (2% / 2mm) as shown in Fig. 5(e) (Υ<1 for all the pixels). More quantitative analysis on fields of 2×2 cm², 4×4 cm², 6×6 cm², 8×8 cm² and 10×10 cm² with depths of 1.5 cm and 10 cm are listed in tables I. All Υ_{pass} reach 100% with 2% / 2mm criteria and exceed 99% for more stringent 1% / 1mm. In comparison, the raw images have mean Υ_{pass} of 80.5% (2% / 2mm) and 61.9% (1% / 1mm) for depth of 1.5 cm, and 87.6% (2% / 2mm) and 60.7% (1% / 1mm) for depth of 10 cm. Υ_{pass} in the raw data are found inversely related to the field size. For example, the mean Υ_{pass} (2%/2mm) is 99.0% for 2 × 2 cm² and reduces to only 47.3% in 10 × 10 cm².

2. Dose prediction for a prostate IMRT case

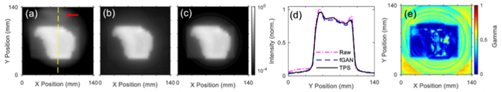

Fig. 6. Dose prediction for a prostate IMRT case (Field 7) at a water depth of 10 cm. (a) The input radioluminescence image collected from our CRIS, (b) predicted dose map, (c) TPS calculation, (d) intensity profiles along the yellow dashed line in (a), and (e) gamma map of the prediction (2% / 2mm). Images are displayed in logscale.

Table II Gamma analysis for prostate IMRT fields.

	Depth	Field 1	Field 2	Field 3	Field 4	Field 5	Field 6	Field 7
1% / 1mm	1.5 cm	88.4%	88.9%	87.7%	88.0%	90.2%	91.4%	87.4%
	10cm	83.5%	75.4%	83.5%	91.4%	86.9%	88.6%	82.9%
2% / 2mm	1.5 cm	99.0%	98.8%	99.3%	99.3%	99.5%	99.1%	99.3%
	10 cm	98.8%	99.4%	98.8%	99.5%	98.5%	99.2%	99.3%

We further investigated a prostate IMRT treatment plan delivered at the gantry angle fixed to 0°, which includes 7 fields with a total of 77 step-and-shot segments. As an example, the predicted dose of the last field at a depth of 10cm is presented in Fig. 6. The mirror-glare artifacts indicated with a red arrow are visible in the position close to that in Fig. 5(a), accounting for a profile deviation of 4% as shown in Fig. 6(d). Figure 6(d) shows the gamma map using 2%/2mm criterion, where moderate deviations on Υ (~0.5) can be found in the low-dose regions surrounding the primary beam. By checking the settings in TPS, these regions are mostly covered by the secondary collimator jaws. The quantitative results of the prostate IMRT plan with 1%/1 mm and 2%/2 mm gamma criteria are summarized in Table II for depths of 1.5 cm and 10 cm. The mean Υ_{pass} for the seven fields are 88.9% (1% / 1mm) and 99.2% (2% / 2mm) for a depth of 1.5 cm, and 84.6% (1% / 1mm) and 98.7% (2% / 2mm) for a depth of 10 cm. No significant differences were observed on Υ_{pass} (2%/2mm) among the seven fields with multiple segments and the open fields in table I.

CONCLUSIONS

In this work, we developed a radioluminescence imaging system and a dose prediction strategy that converts the measured radioluminescence image to dose maps using a flexible deep learning model. Leveraged from the cylindrical receptor structure, our system allows for dosimetric measurement from any gantry angle. The proposed deep learning model enables robust domain transformation from CRIS image to dose maps at multiple depths, which makes it possible to predict 3D dose distribution. The proposed fGAN model outperforms other state-of-the-arts deep learning models in this specific application. Validation experiments were performed for five square fields (ranging from 2 × 2 cm² to 10 × 10 cm²), and a clinical prostate IMRT case (total of 77 step-and-shoot segments). The results were compared to the TPS calculations in terms of gamma index at 1.5 cm, 5 cm and 10 cm depths. The mean 2% / 2mm gamma pass rates were 100% for square fields and 98.3% (range from 97.5% to 99.5%) for the irregular IMRT fields. The system is demonstrated to be a promising and cost-effective alternative to the current EPID-based dosimetry.

ACKNOWLEDGEMENTS

The authors acknowledge the funding supports from the National Cancer Institute (1R01CA223667 and 1R01CA227713).

REFERENCES

1. **L. Xing**, et. al., "Visualizing Radiation Therapy Beam in Real-Time in the context of Patient's Anatomy," ed: Google Patents, 2017.
2. **J. Cesare**, et al. "Automating quality assurance of digital linear accelerators using a radioluminescent phosphor coated phantom and optical imaging." Physics in Medicine & Biology 61.17 (2016): L29.

CONTACT INFORMATION

Department of Radiation Oncology @ Stanford University

Jeremy18@stanford.edu